Article

CFD Investigation into Influences of a Transversely and Periodically Deforming Microchannel on Shear Stress Behavior in a Gut-on-a-chip Device

Pannasit Borwornpiyawat[1,a], Ekachai Juntasaro[1,b,*], Sasitorn Aueviriyavit[2], Varangrat Juntasaro[3], Witsaroot Sripumkhai[4], Pattaraluck Pattamang[4], Rattanawan Meananeatra[4], Kornphimol Kulthong[2], Ratjika Wongwanakul[2], Numfon Khemthongcharoen[5], Panut Bumphenkiattikul[6], Arthit Vongachariya[6], Nithi Atthi[4], and Wutthinan Jeamsaksiri[4]

1 Mechanical Engineering Simulation and Design Group, The Sirindhorn International Thai-German Graduate School of Engineering (TGGS), King Mongkut's University of Technology North Bangkok (KMUTNB), Bangkok 10800, Thailand
2 Nano Safety and Bioactivity Research Team, National Nanotechnology Center (NANOTEC), National Science and Technology Development Agency (NSTDA), Pathum Thani 12120, Thailand
3 Department of Mechanical Engineering, Kasetsart University, Bangkok 10900, Thailand
4 Thai Microelectronics Center (TMEC), National Electronics and Computer Technology Center (NECTEC), National Science and Technology Development Agency (NSTDA), Chacheongsao, 24000, Thailand
5 National Electronics and Computer Technology Center (NECTEC), National Science and Technology Development Agency (NSTDA), Pathum Thani 12120, Thailand
6 Simulation Technology, Digital Manufacturing, SCG Chemicals Public Company Limited, Bangkok 10800, Thailand

E-mail: [a]s6009091960018@email.kmutnb.ac.th, [b,*]ekachai.j@tggs.kmutnb.ac.th (Corresponding author)

Abstract. Organ-on-a-chip allows dynamic microenvironment of the actual organ to be simulated in vitro. In this study, the CFD simulation is used to investigate the behaviors of fluid flow and shear stress due to the effect of a transversely deforming membrane caused by the cyclic deformation of the microchannel sidewalls in a gut-on-a-chip device. The result reveals that the shear stress varies linearly along the length of the microchannel. The average shear stress per cycle is approximately three times greater than that of the stationary microchannel. The amplitude and frequency of the cyclic deformation also significantly affect the flow and shear stress behaviors. The highly dynamic shear stress in the gut-on-a-chip device could be one of the major factors that makes this kind of device more viable than the traditional static cell culture.

Keywords: Gut-on-a-chip, shear stress, deforming microchannel, CFD, simulation.

1. Introduction

Organs-on-chips are microfluidic devices that allow recreation of key physiological functions of organs [1]–[3] such as lung [4], intestine (gut) [5], liver [6], kidney [7], or even multiple organ systems such as intestine-liver [8], blood-brain [9], intestine-liver-skin-kidney [10], and other combinations of organs [11]–[16]. The features that most organs-on-chips devices have in common are the microchannels that are separated by the porous membrane where the cells of interest are cultured upon. The microchannels are perfused with a liquid medium in order to mimic the dynamic environment of nutrient flow and blood circulation. In some advanced devices, the cell culture can be further stimulated by exerting the cyclic deformation on the membrane, where cells are adhered to, in order to mimic the peristalsis motion of the actual organ [4], [5], [17]–[19].

Among these organs, the intestine is the major absorption site for foods as well as drugs taken orally [20], which is the most preferred route of administration [21]. Kim et. al. (2012) was the first group who developed a gut-on-a-chip device, which was able to closely replicate the behavior and features of human intestine, using the Caco-2 cells. The keys for this accomplishment are the shear stress caused by fluid flow within the device's microchannels, at the volume flow rate of 30 µL/h that generates the shear stress of 0.02 dyne/cm², together with the cyclic mechanical strain on the membrane due to its deformation, which is equal to 10% at the frequency of 0.15 Hz [5]. Previous studies confirmed that the intestinal cells cultured in the dynamic environment of gut-on-a-chip devices rapidly developed and exhibited better characteristic, compared to the conventional static cell culture models [22]–[25]. The shear stress of 0.02 dyne/cm² has become widely accepted as the optimal value to maintain in the gut-on-a-chip applications during the differentiation and polarization stages of the Caco-2 cells [26], even though the underlying mechanism is still not fully discovered and not clearly understood until this day [27]. It is also believed that the effect of membrane cyclic deformation on the fluid flow is negligible due to the low frequency of periodically deforming membrane and the small size of microchannels [28]. However, the shear stress is a function of the flow velocity, the fluid viscosity and the geometry of the flow passage [29]–[31]. This means that even though the fluid flows into the device at a constant flow rate, if the geometry of the flow passage changes, the shear stress will change accordingly. The characteristic of Caco-2 cells was reported by Delon et al. (2019) to change differently depending on the shear stress ranges from 0.01 to 0.03 dyne/cm². The study was carried out using the microchannel that was narrower on one side and wider on the other side to generate the shear stress that varied linearly along the length of microchannel [32]. However, so far there has been no detailed study on the behaviors of flow and shear stress within the gut-on-a-chip device, especially when subjected to the cyclic deformation of the membrane and microchannels.

In this study, the temporal and spatial behaviors of the shear stress in the gut-on-a-chip device subjected to the cyclic deformation in the transverse direction are investigated using the CFD simulation. The goal is to establish the understanding of the flow pattern as well as the shear stress characteristic within the device, which might be the key factors that make this dynamic gut-on-a-chip model superior to the traditional static models, so that it will be beneficial for researchers who are interested in the gut-on-a-chip as well as other organs-on-chips applications.

2. Materials and Methods

2.1. Governing Equations

In order to study the flow and shear stress behaviors in the gut-on-a-chip device, ANSYS Fluent Academic version 2019R3 is used to perform the CFD simulation. The flow is governed by the continuity equation and the Navier-Stokes equations as follows:

$$\nabla \cdot \vec{\mathbf{u}} = 0 \tag{1}$$

$$\frac{\partial \vec{\mathbf{u}}}{\partial t} + (\vec{\mathbf{u}} \cdot \nabla)\vec{\mathbf{u}} = -\frac{1}{\rho}\nabla P + \nu\nabla^2\vec{\mathbf{u}} \tag{2}$$

where $\vec{\mathbf{u}}$ is the velocity vector, t is the time, ρ is the fluid density, P is the pressure and ν is the fluid kinematic viscosity.

The shear stress, τ_w, is the stress due to the shear force of the fluid flow acting on the surface of interest in the direction parallel to the flow which can be described as

$$\tau_w = \mu\frac{\partial u}{\partial y}\bigg|_{y=0} \tag{3}$$

where μ is the fluid dynamic viscosity.

In case of flow in a rectangular microchannel, a simplified equation for calculating shear stress can be expressed [33]–[35] as

$$\tau_w = \frac{6\mu Q}{WH^2} \tag{4}$$

where Q is the volume flow rate, W is the width of microchannel and H is the height of microchannel. However, the shear stress from Eq. (4) is the average shear stress over a cross section of microchannel at any given volume flowrate. For this reason, it is only used to determine the fluid dynamic viscosity in this study. In order to determine the local shear stress, especially when the microchannel deforms and the flow is disturbed, Eq. (3) is more appropriate and therefore is used to calculate the shear stress in this study.

The problem is solved by the finite volume method, using the transient pressure-based solver for laminar flow since the fluid density is constant and the Reynolds number in this problem is very low, i.e. $Re \approx 0.016$, which can be calculated from

$$Re = \frac{\rho U D_h}{\mu} \qquad (5)$$

where U is the mean flow velocity and D_h is the hydraulic diameter of the flow passage.

2.2. Discretization Schemes

The pressure and velocity are coupled using the SIMPLE algorithm, which employs the continuity equation, i.e. Eq. (1), to ensure that the mass is conserved throughout the calculation. The algorithm was originally developed by Patankar and his colleagues in 1970s [36]. The discretization schemes for both temporal and spatial derivatives in the Navier-Stokes equations, i.e. Eq. (2), used in this study are explained as follows:

Let ϕ be a general scalar variable. The second-order implicit time integration scheme is used for the calculation of temporal derivatives as

$$\frac{\partial \phi}{\partial t} = \frac{3\phi^{M+1} - 4\phi^M + \phi^{M-1}}{2\Delta t} \qquad (6)$$

where the subscript M+1 is the value at the next time step, the subscript M is the value at the current time step, the subscript M-1 is the value at the previous time step and Δt is the size of time step.

For spatial derivatives, there are typically three terms in the Navier-Stokes equations to be considered: the convection term, the pressure term and the diffusion term. For the convection term, the value of a quantity at the control volume surface, ϕ_f, is calculated using the second-order upwind differencing scheme as

$$\phi_f = \phi_{up} + \nabla\phi_{up} \cdot \vec{r}_{up} \qquad (7)$$

where ϕ_{up} is the value in the upstream control volume, $\nabla\phi_{up}$ is the gradient of the quantity ϕ_{up} in the upstream control volume and $\vec{r}_{up}$ is the displacement vector from the upstream control volume to the control volume surface that is being calculated.

For the pressure-gradient and diffusion terms, the second-order central differencing scheme is used and ϕ_f is calculated by

$$\phi_f = \frac{1}{2}(\phi_{c_a} + \phi_{c_b}) + \frac{1}{2}(\nabla\phi_{c_a} \cdot \vec{r}_{c_a} + \nabla\phi_{c_b} \cdot \vec{r}_{c_b}) \qquad (8)$$

where ϕ_{c_a} and ϕ_{c_b} are the values in the control volumes on both sides of the surface, $\nabla\phi_{c_a}$ and $\nabla\phi_{c_b}$ are the gradients of ϕ_{c_a} and ϕ_{c_b} respectively, $\vec{r}_{c_a}$ is the displacement vector from the control volume "a" to the

surface that is being calculated and $\vec{r}_{c_b}$ is the displacement vector from the control volume "b" to the same surface.

The variable ϕ in Eq. (6) – Eq. (8) can be the x-velocity, the y-velocity, the z-velocity or the pressure depending on what is being calculated at that moment. Furthermore, the gradient terms in Eq. (7) and Eq. (8) are evaluated using the least squares cell-based method which assumes a linear variation of ϕ between the control volume of interest and its neighboring control volumes. In order to determine the gradient of ϕ in the control volume, $(\nabla\phi)_{c_0}$, a linear system of equations is solved in a least squares manner as follows:

$$[J](\nabla\phi)_{c_0} = [\Delta\phi_i] \qquad (9)$$

where J is the coefficient matrix depending on the geometry of the control volumes and $\Delta\phi_i$ is the matrix containing the difference of ϕ between the control volume of interest and each neighboring control volume [37].

2.3. Domain, Boundary Conditions and Case Studies

The device prototype has two identical main microchannels, each of which has the height of 150 μm and the width of 1,000 μm, separated by a 30-μm-thick membrane. The upper and lower microchannels together with the membrane in the middle are positioned between two vacuum chambers on both sides. When the pressure in vacuum chambers is reduced, the membrane as a common wall of both upper and lower microchannels is stretched in the transverse direction to the main flow as shown in Fig. 1.
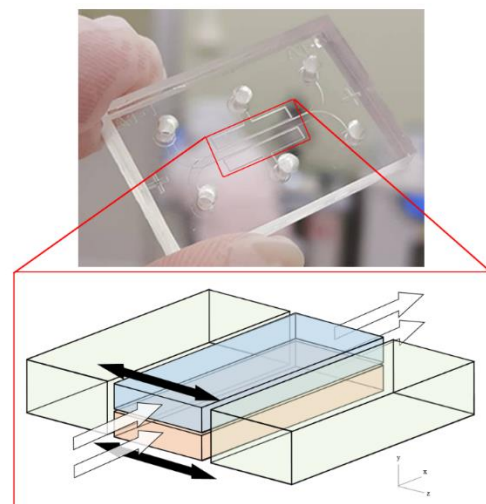
Fig. 1. Device prototype fabricated with PDMS and the illustration of the cell culture area within the device. The main microchannels are shown in blue (upper) and orange (lower). Two vacuum chambers are shown in green (far left and far right). The white arrows indicate the main flow direction and the black arrows indicate the deforming direction.

In this study, only a quarter of the upper microchannel is considered as a simulation domain because it is symmetrical in both y and z directions. The symmetry boundary condition is imposed on the xy-plane (yellow), which is located in the middle of the upper microchannel, as well as the top surface at y = H = 75 µm, which is located at the half-height of the upper microchannel. The bottom surface (grey), where the cells are cultured, is specified as the no-slip wall condition. The side surface (blue) is also specified as the no-slip wall condition but is subjected to the oscillation movement in the z-direction where its original position is located at z = W = 500 µm. The inlet and outlet are located at x = 0 and x = L = 1 cm respectively, as shown in Fig. 2.
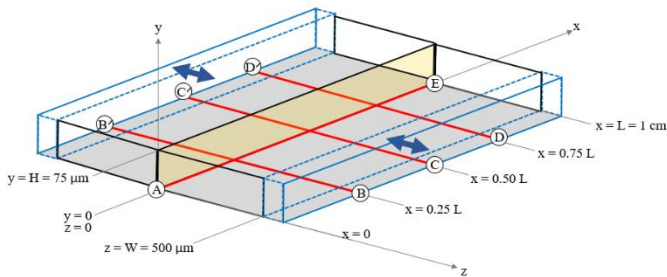
Fig. 2. The simulation domain with its reflection at the xy-plane. The red lines indicate the plot locations for shear stress.

It is assumed that the sidewall moves and oscillates as a rigid body and its motion is modeled using the dynamic mesh user-defined function (UDF) as described by Eq. (10) for its displacement and Eq. (11) for its velocity [38].

$$S_D(t) = \frac{1}{2}\varepsilon\left(1 - \cos(2\pi f \cdot t)\right) \qquad (10)$$

$$S_V(t) = \frac{\pi f \varepsilon \sin(2\pi f \cdot t)}{\max\left(\frac{dS_D(t)}{dt}\right)} \qquad (11)$$

where ε is the mechanical strain and f is the frequency of cyclic deformation. The temporal behaviors of the displacement and velocity of the sidewall during a deformation cycle are shown in Fig. 3.
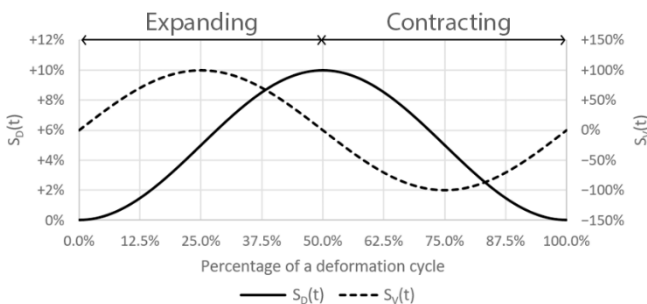
Fig. 3. Plots of sidewall displacement and velocity during a deformation cycle with ε = 10% and f = 0.15 Hz.

The simulation is performed for five different cases using the same domain as shown previously in Fig. 2. In

this study, the fluid density is 997.0 kg/m³, which is equal to that of water at 37°C [39], and the dynamic viscosity is 9.0×10^{-4} Pa·s which is calculated from Eq. (4) with the parameters reported in Kim et al. (2012). The different boundary conditions are used in different cases as summarized in Table 1. Case A serves as the reference case where only the fluid flow is present without domain deformation. Case B is the contrast where the main flow is absent while the domain deforms according to the prescribed motion of the sidewall. Case C is what actually happens in the device where both the main flow and the domain deformation are present. Cases D and E are considered to further investigate the flow and shear stress behaviors in the device by doubling the mechanical strain and frequency from Case C respectively.

Table 1. Summary of boundary conditions used in different cases in this study.

Case	A	B	C	D	E
Main flow	Yes	No	Yes	Yes	Yes
Inlet BC*	Q = 7.5 µL/h	P = 0 Pa	Q = 7.5 µL/h	Q = 7.5 µL/h	Q = 7.5 µL/h
Outlet BC	P = 0 Pa				
Side wall motion	No	Yes	Yes	Yes	Yes
ε	-	10%	10%	20%	10%
f	-	0.15 Hz	0.15 Hz	0.15 Hz	0.30 Hz

*The volume flow rate of 7.5 µL/h in this study is equivalent to 30 µL/h as reported in Kim et al. (2012)

The area-weighted average shear stress, $\overline{\tau_w}$, at the bottom surface in each case is computed by

$$\overline{\tau_w} = \frac{\sum_{i=1}^{n}\left(\tau_{w_i} \cdot A_i\right)}{\sum_{i=1}^{n}(A_i)} \qquad (12)$$

where n is the number of control volumes at the bottom surface, τ_{w_i} is the shear stress of each control volume at the bottom surface, calculated from Eq. (3), and A_i is the surface area of each individual control volume at the bottom surface.

For Cases B – E, which are time-dependent, Eq. (12) is used to compute $\overline{\tau_w}$ at every time point in the simulation and, when each cycle is complete, $\overline{\tau_w}$ is used to compute the time-averaged shear stress as

$$\overline{\overline{\tau_w}} = \frac{1}{T}\sum_{j=1}^{N}\left[\frac{\left(\overline{\tau_{w_j}} + \overline{\tau_{w_{j-1}}}\right)}{2} \cdot \Delta t\right] \qquad (13)$$

where N is the number of time steps in a cycle, $\overline{\tau_{w_j}}$ and $\overline{\tau_{w_{j-1}}}$ are calculated from Eq. (12) at the current and

previous time points respectively, Δt is the size of time step and $T = 1/f$. The area-weighted average equivalent volume flow rates, $\overline{Q_o}$, and the time-averaged equivalent volume flow rates, $\overline{\overline{Q_o}}$, at the outlet are calculated in the same manner.

3. Grid-independent Analysis and Time-step-size Verification

The grid-independent study is carried out in Case C using three different grid levels as shown in Table 2. The representative grid size, Δs, of each grid level is calculated by

$$\Delta s = \left(\frac{\Delta V}{n}\right)^{\frac{1}{3}} \tag{13}$$

where ΔV is the domain volume and n is the total number of control volumes in the domain. The initial size of the time step, Δt_{init}, is calculated based on the CFL convergence condition [40] as

$$\Delta t_{init} = \frac{\Delta s}{U} \tag{14}$$

where $U = 55.5556$ μm/s in this study.

Table 2.   Summary of different grid levels in this study.

Grid level		Coarse	Medium	Fine
ΔV (μm³)		3.75×10⁸		
Directional grid size	Δx (μm)	200	100	50
	Δy (μm)	15	10	5
	Δz (μm)	15	10	5
n		8,500	40,000	300,000
Δs		35.3349	21.0858	10.7722
Δt_{init}		0.6360	0.3796	0.1939

The size of the initial time step in Table 2 is then adjusted such that when multiplied by the number of time steps per cycle, N, the resulting multiplication is always equal to the cycle time period, T. The smaller sizes of the time step are also used together with their corresponding number of time steps per cycle, as summarized in Table 3, to further observe any change that may happen. The simulation is performed for at least three cycles to ensure that the results are converged.

In order to find the optimum grid level and size of time step to be used in this study, first, the smallest Δt of those adjusted from Δt_{init}, i.e. $\Delta t = 0.1111$ s, is used in the preliminary simulation for all three grid levels. Then, the area-weighted average shear stress at the bottom surface, $\overline{\tau_w}$, and the area-weighted average equivalent volume flow rate at the outlet, $\overline{Q_o}$, are plotted as shown in Fig. 4 and Fig. 5 respectively.

Table 3.   The size of time step and the number of time steps per cycle used in the grid-independent study.

Cycle time period, T (s)	Size of time step, Δt (s)	Number of time steps per cycle, N
6.6667	0.6667*	10
	0.3333*	20
	0.1111*	60
	0.0556	120
	0.0185	360

*Adjusted from Δt_{init} in Table 2.
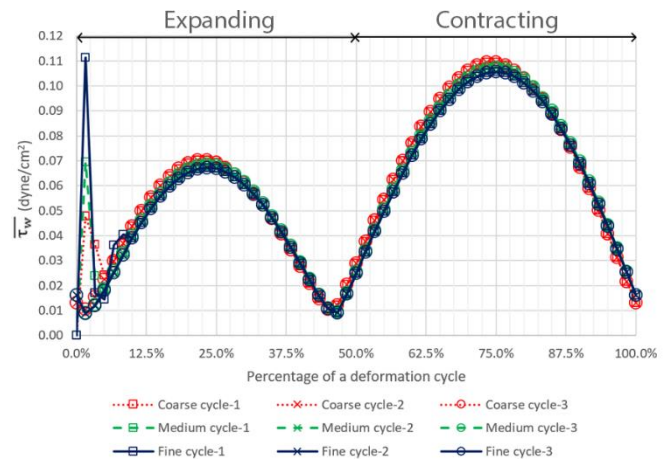
Fig. 4. Plots of the area-weighted average shear stress at the bottom surface in each cycle, using three different grid levels with $\Delta t = 0.1111$ s.
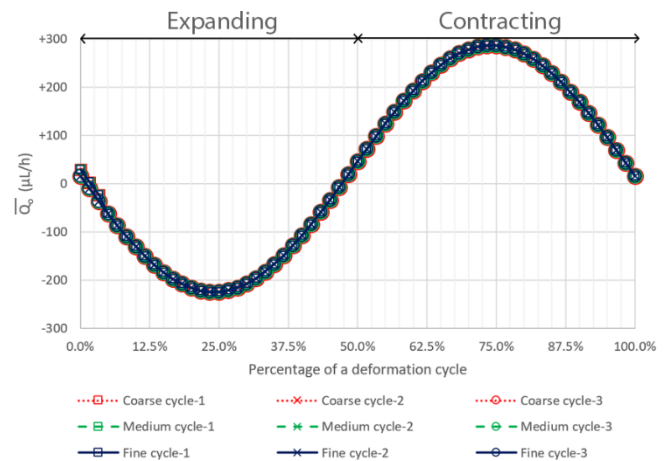
Fig. 5. Plots of the area-weighted average equivalent volume flow rate at the outlet in each cycle, using three different grid levels with $\Delta t = 0.1111$ s.

It can be seen from Fig. 4 that there appears a sharp peak in the shear stress at the beginning of cycle-1 on all three grid levels. This is due to the initialization of the solver which requires some iterations before the solutions become smooth. The solution from the same grid level in each cycle is plotted on top of each other to make it easier to observe any variation between cycles. The

equivalent volumetric flow rate in Fig. 5 exhibits similar behavior in the first cycle, even though the peak is so small that it is almost unnoticeable.

In both Fig. 4 and Fig. 5, the results from cycle-2 and cycle-3 are aligned perfectly which indicate that three cycles are sufficient for the simulation. The time-averaged shear stresses, $\overline{\overline{\tau_w}}$, and equivalent volume flow rates, $\overline{\overline{Q_o}}$, for each grid level are summarized in Table 4 along with the relative errors between two consecutive grid levels.

Table 4. The time-averaged shear stresses and equivalent volume flow rates in three different grid levels with Δt = 0.1111 s.

Grid level	Coarse	Medium	Fine
$\overline{\overline{\tau_w}}$ (dyne/cm²)	0.0601	0.0590	0.0583
%Error	-	1.7523%	1.2123%
$\overline{\overline{Q_o}}$ (µL/h)	30.1807	30.1827	30.1833
%Error	-	0.0066%	0.0021%

The medium grid is thus used to verify the size of the time step by performing additional simulations with two smaller time step sizes in order to calculate $\overline{\overline{\tau_w}}$ and $\overline{\overline{Q}}$ as summarized in Table 5.

Table 5. The time-averaged shear stresses and equivalent volume flow rates in medium grid level with different sizes of time step.

Δt (s)	0.1111	0.0556	0.0185
$\overline{\overline{\tau_w}}$ (dyne/cm²)	0.0590	0.0589	0.0586
%Error	-	0.1370%	0.5558%
$\overline{\overline{Q_o}}$ (µL/h)	30.1827	30.0464	30.0051
%Error	-	0.4515%	0.1375%

From grid-independent analysis and time-step-size verification, it is confirmed that the medium grid with Δt = 0.0556 s and three cycles of the sidewall deformation are sufficient to obtain the converged solution for this study.

4. Results and Discussion

4.1. Primary Flow in the Stationary Microchannel

In Case A, a constant flow rate in the stationary microchannel produces the very smooth flow pattern and uniformly distributed shear stress throughout the microchannel as can be seen by the streamlines and velocity vectors in Fig. 6 and the contour of shear stress in Fig. 7. Moreover, the shear stress profiles at four different locations, i.e. along the AE, BB′, CC′ and DD′

lines, are shown in Fig. 8 to better visualize the shear stress distribution in this case.
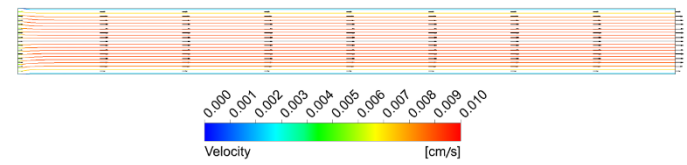
Fig. 6. Streamlines (colorized) and velocity vectors (black) at the top surface in Case A.
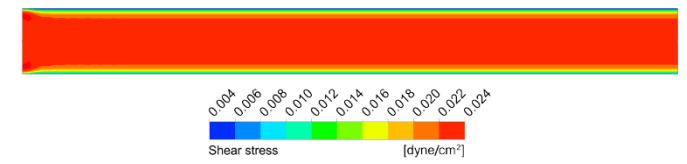
Fig. 7. Contour of shear stress at the bottom surface in Case A.
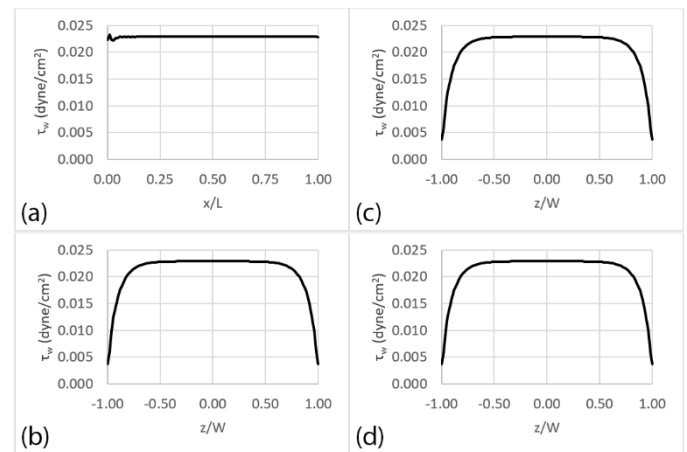
Fig. 8. Plots of shear stress in Case A at four different locations: (a) AE line, (b) BB′ line, (c) CC′ line and (d) DD′ line. The plot locations are shown in Fig. 2.

The leftmost areas of Fig. 6 and Fig. 7 are affected by the fixed inlet boundary condition. This effect is also visible in Fig. 8(a) where small numerical oscillation can be seen at x/L < 0.1. This is due to the insufficiently fine mesh locally near the inlet in this case. However, the mesh is used regardless of this numerical oscillation in order to preserve the uniformity and consistency of the meshes in all cases. This effect should not be taken into account when interpreting the results in this case.

The profiles of shear stress in Fig. 8(b), (c) and (d) are identical because there is no disturbance in the flow field. The shear stress at the center of the microchannel, i.e. $|z/W| \leq 0.5$, is not affected by the sidewalls and the magnitude is equal to 0.0229 dyne/cm². However, the wall shear stress in the outer region, i.e. $0.5 < |z/W| \leq 1.0$, drastically decreases as approaching the sidewalls. The further analysis of the shear stress in this region reveals that the difference between the maximum and local shear stresses is an exponential function of the dimensionless transverse distance, $\tau_{w,max} - \tau_w = Ae^{B|z/W|}$ where A = 5×10⁻⁷ and B = 10.606, as can be seen in Fig. 9. At $|z/W|$ = 1.0, the shear stress is 0.0036

dyne/cm², which is approximately 6 times lower than that at the center. The area-weighted average shear stress on the bottom surface, $\overline{\tau_w}$, is 0.0210 dyne/cm² in this case.
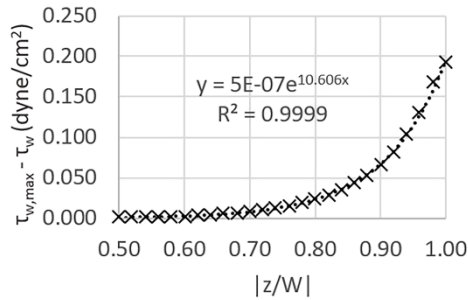
Fig. 9 Plot of the difference between maximum and local shear stresses at $0.5 < |z/W| \leq 1.0$ in Case A.

4.2. Secondary Flow due to the Deforming Surfaces

The flow in Case B occurs solely because of the motion of the sidewalls, which expand and contract as a function of time. The fluid is drawn toward the center of the device when the sidewalls are expanding and then squeezed through both ends of the device when the sidewalls are contracting. In order to visualize the flow field and shear stress distribution in this case, the streamline and velocity vectors are shown in Fig. 10 and the contour of shear stress is shown in Fig. 11 at nine different time points in a deformation cycle. The top and bottom horizontal lines shown in magenta indicate the original positions of the sidewalls.
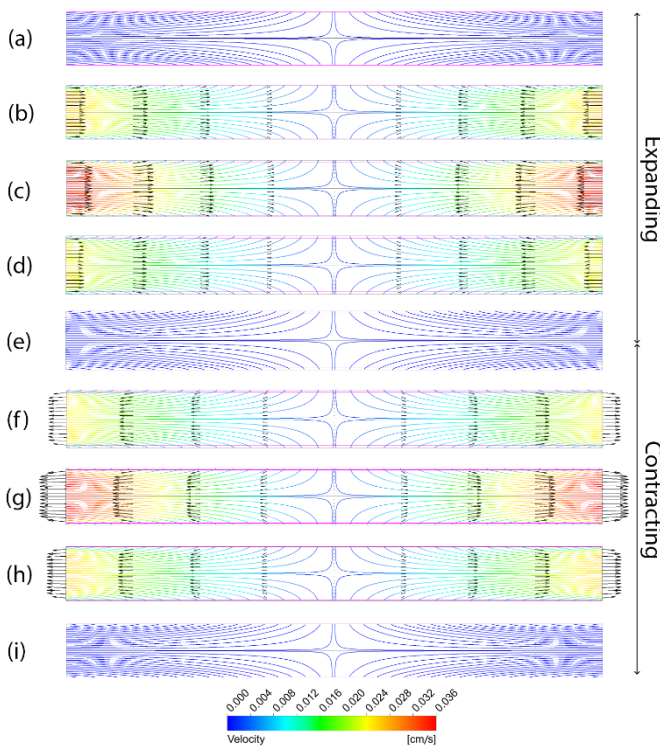
Fig. 10 Streamlines (colorized) and velocity vectors (black) at the top surface in Case B at nine different time points (a – i) during a deformation cycle.
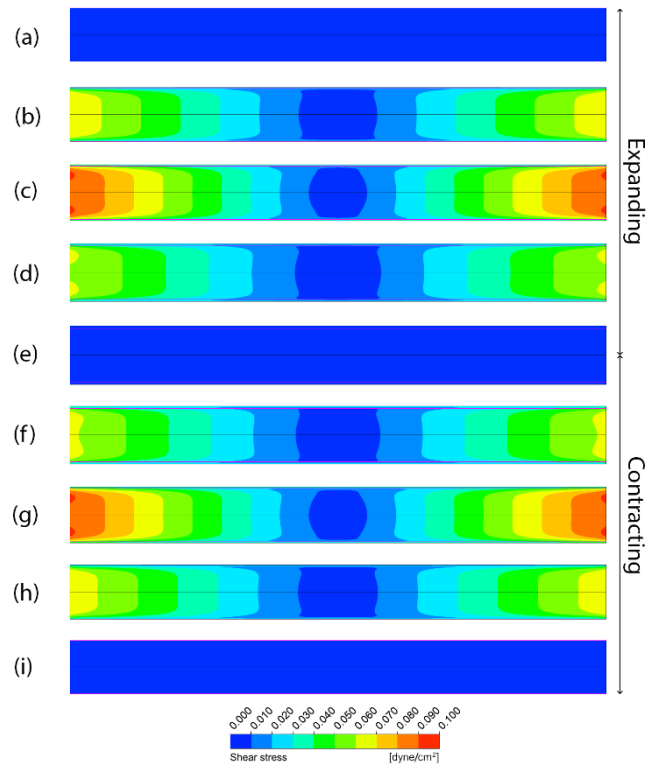
Fig. 11 Contours of shear stress at the bottom surface in Case B at nine different time points (a – i) during a deformation cycle.

The oscillating movement of the sidewalls in the transverse direction induces the symmetrical flow pattern as can be seen by the streamlines in Fig. 10. The farther the position away from the center of the device, the higher the flow velocity and hence the greater the shear stress compared to that at the center as can be seen by the contours in Fig. 11. It should be noted that, at the same position of the sidewalls during a deformation cycle, the distribution of shear stress is not identical. This can be seen clearly in Fig. 11(d) and (f) where the sidewalls are at 75% of the maximum deformation in both figures but the former is during the expansion while the latter is during the contraction. The other pairs, i.e. Fig. 11(c) and (g) as well as Fig. 11(b) and (h), are also different from each other but less noticeable. The shear stress profiles along the AE, BB′, CC′ and DD′ lines are shown in Fig. 12 – Fig. 15 respectively for detailed analysis.
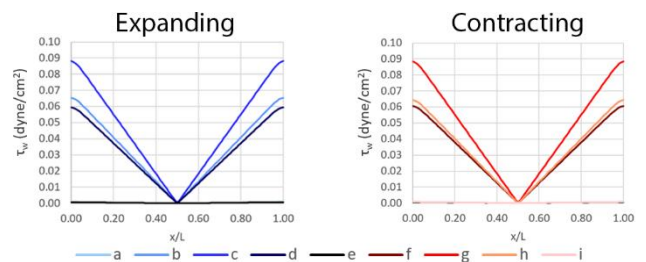
Fig. 12. Plots of shear stress in Case B along the AE line at nine different time points (a – i) during a deformation cycle.
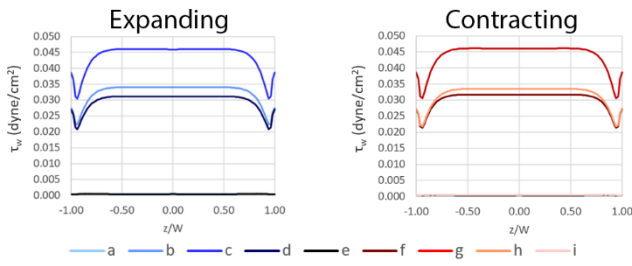
Fig. 13. Plots of shear stress in Case B along the BB′ line at nine different time points (a – i) during a deformation cycle.
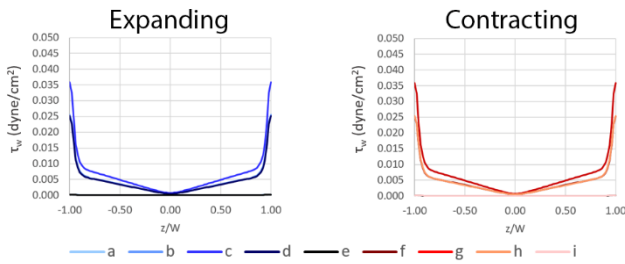
Fig. 14. Plots of shear stress in Case B along the CC′ line at nine different time points (a – i) during a deformation cycle.
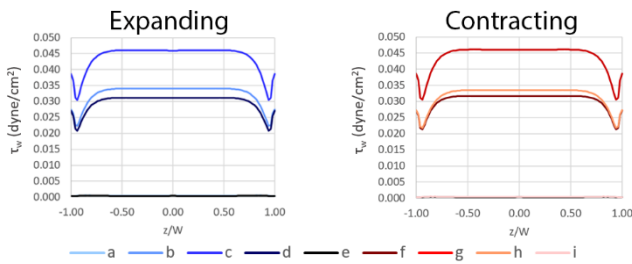
Fig. 15. Plots of shear stress in Case B along the DD′ line at nine different time points (a – i) during a deformation cycle.

The observation of the shear stress profiles at different positions and time points leads to the deeper understanding of the shear stress behavior due to the membrane deformation, especially when the sidewalls are expanding and contracting.

In Fig. 12, the shear stress has the V-shape profiles, which indicate the linear relationship between the shear stress and the position along the AE line. The local shear stress due to the flow induced by the transverse deformation can reach up to 0.0881 dyne/cm² as can be seen at time point c during the expansion and at time point g during the contraction, when the sidewalls move at the maximum velocity.

In Fig. 13, the distribution of shear stress along the BB′ line is relatively constant in the center area where $|z/W| \leq 0.5$ and the shear stress gradually decreases where $0.5 < |z/W| \leq 0.95$. The shear stress increases again when $|z/W| > 0.95$ because the flow starts to change the direction from parallel to perpendicular to the bottom surface in this area.

In Fig. 14, the shear stress has the U-shape profiles, which share similarity between the profiles in Fig. 12 and Fig. 13. The profiles have the linear variation where

$|z/W| \leq 0.85$ which is similar to those in Fig. 12 although the magnitude of shear stress in Fig. 14 is much lower because the velocity along the CC′ line is almost zero. When $|z/W| > 0.85$, the wall shear stress abruptly increases due to the deviation of the flow direction, similar to those in Fig. 13.

In Fig. 15, the shear stress profiles are identical to those in Fig. 13, except that the flow is in the opposite direction.

Additionally, it should be noted here that the shear stress is zero across the domain when the sidewalls are at the original position (time point a and i) and at the maximum deformation (time point e).

In this case, the area-weighted average shear stress at the bottom surface, $\overline{\tau_w}$, is plotted in Fig. 16 and the time-averaged shear stress at the bottom surface during a deformation cycle, $\overline{\overline{\tau_w}}$, is 0.0282 dyne/cm². Furthermore, it can be observed that there are small phase shifts between the time points where the sidewalls are at the maximum velocity and the time points where the maximum shear stress occur, as indicated by the vertical lines shown in red and blue respectively.
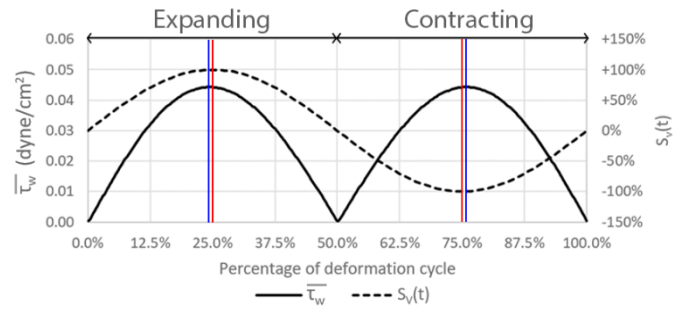
Fig. 16 Plot of area-weighted average shear stress at the bottom surface and the sidewalls velocity during a deformation cycle in Case B. The vertical lines shown in red and blue indicate the time points where maximum sidewalls velocity and shear stress occur respectively.

4.3. Flow and Shear Stress Behaviors in the Gut-on-a-chip Device

In Case C, the fluid flows into the device at a constant flow rate while the moving sidewalls of the main microchannels in the device expand and contract in cycles. The primary flow is disturbed by the deformation of the microchannels that moves in the transverse direction to the primary flow. This alters the flow field and shear stress distribution within the device. In order to visualize the flow field and shear stress distribution in this case, the streamlines together with velocity vectors are shown in Fig. 17 and the contours of shear stress are shown in Fig. 18 at nine different time points in a deformation cycle.
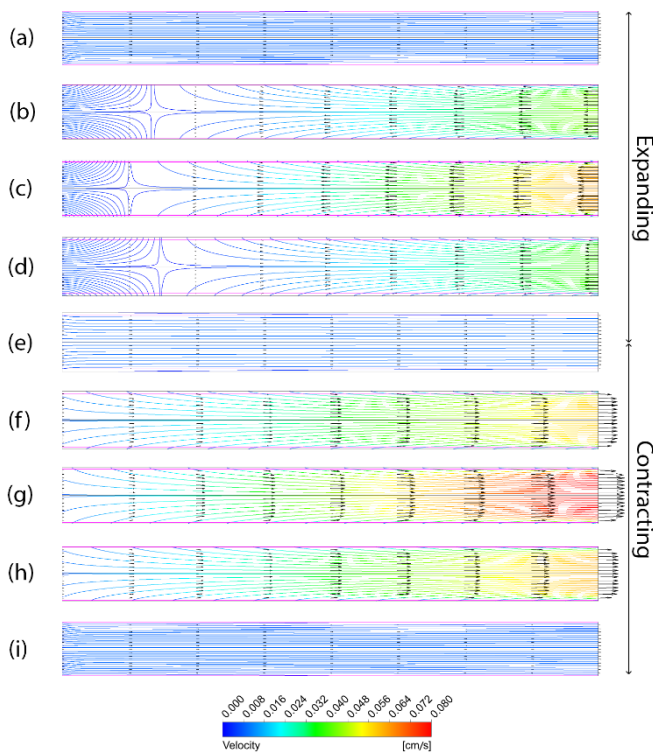
Fig. 17 Streamlines (colorized) and velocity vectors (black) at the top surface in Case C at nine different time points (a – i) during a deformation cycle.
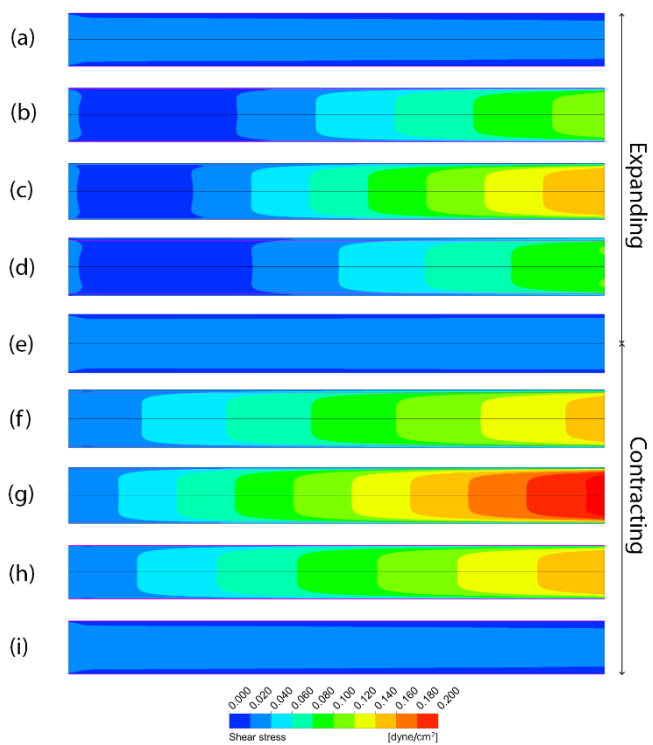
Fig. 18 Contours of shear stress at the bottom surface in Case C at nine different time points (a – i) during a deformation cycle.

At the beginning of the cycle where the sidewalls are at the original position, the fluid flows directly from the inlet on the left to the outlet on the right as indicated by relatively straight streamlines in Fig. 17(a). During the expansion as shown in Fig. 17(b) – (d), the fluid is drawn

back into the device from the outlet side while the constant flow from the inlet side tries to push the fluid out of the device. This creates the stagnation point in the flow field as indicated by the deflection of streamlines toward the sidewalls and the flow velocity becomes zero at this point. Once the sidewalls are fully expanded, the stagnation point disappears and the fluid starts to flow out of the device as can be seen in Fig. 17(e). During the contraction, the fluid is accelerated toward the outlet and the flow velocity increases in the streamwise direction as can be seen in Fig. 17(f) – (h) before the sidewalls return to the original position in Fig. 17(i).

The contours of shear stress at the corresponding time points shown in Fig. 18 reveal that the shear stress is distributed almost evenly across the microchannel when the sidewalls are at the original position as well as at the maximum deformation as can be seen in Fig. 18(a), (e) and (i). However, the sidewalls stay at these positions only for a brief moment and then move in either an expanding or contracting manner that generates gradient of shear stress in streamwise direction as can be seen in Fig. 18(b) – (d) and (f) – (h). The shear stress profiles along the AE, BB′, CC′ and DD′ lines in this case are shown in Fig. 19 – Fig. 22 respectively for further analysis.
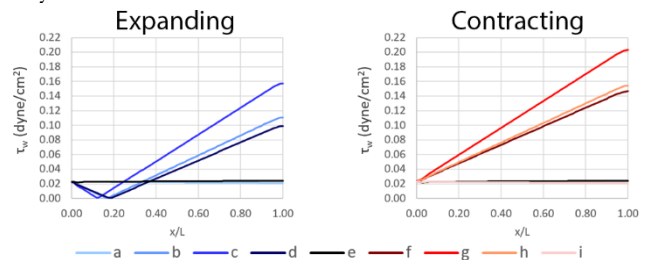
Fig. 19. Plots of shear stress in Case C along the AE line at nine different time points (a – i) during a deformation cycle.
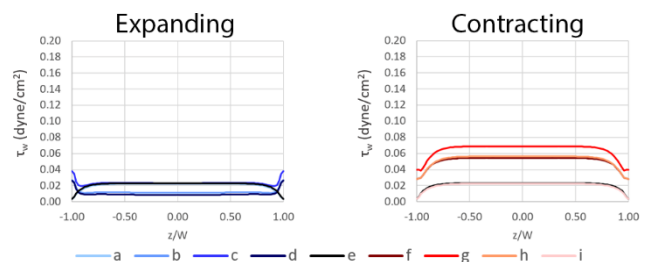
Fig. 20. Plots of shear stress in Case C along the BB′ line at nine different time points (a – i) during a deformation cycle.
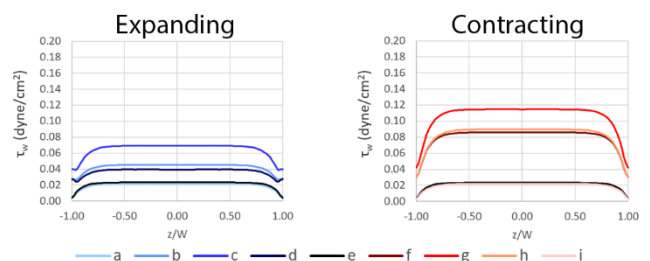
Fig. 21. Plots of shear stress in Case C along the CC′ line at nine different time points (a – i) during a deformation cycle.
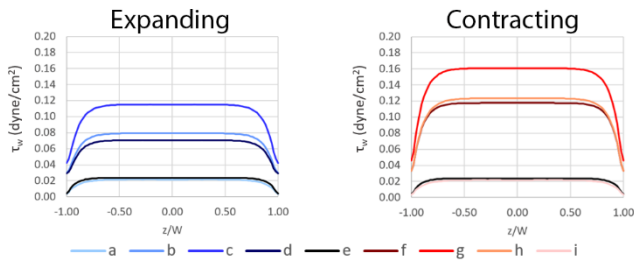
Fig. 22. Plots of shear stress in Case C along the DD′ line at nine different time points (a – i) during a deformation cycle.

In Fig. 19, it is revealed that the shear stress in the streamwise direction starts off at 0.02 dyne/cm² from the inlet at x/L = 0. During the expansion, the shear stress decreases to zero at the stagnation point before linearly increases as approaching the outlet at x/L = 1. During the contraction, the shear stress increases monotonically along the flow path up to 0.20 dyne/cm² as can be seen at time point g, which is ten times greater than that at the inlet, as well as when the sidewalls are stationary.

In Fig. 20 – Fig. 22, the shear stress profiles are similar at most time points and locations, with increasing magnitude along the microchannel length. Except for Fig. 20 at time points b – d, which are in close proximity to the stagnation point during the expansion of the sidewalls. At these particular time points, the shear stress in the center area of the device is lower than that near the sidewalls.

In this case, the area-weighted average shear stress at the bottom surface, $\overline{\tau_w}$, is plotted in Fig. 23 and the time-averaged shear stress at the bottom surface during a deformation cycle, $\overline{\overline{\tau_w}}$, is 0.0589 dyne/cm². Similar to Case B, small phase shifts between the time points where maximum sidewall velocities and maximum shear stress occur can be noticed.
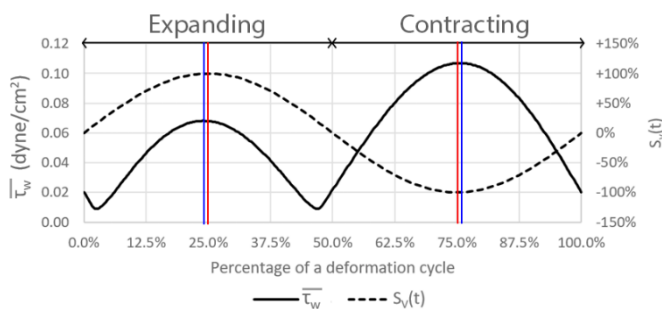
Fig. 23 Plot of area-weighted average shear stress at the bottom surface and the sidewalls velocity during a deformation cycle in Case C. The vertical lines shown in red and blue indicate the time points where maximum sidewalls velocity and shear stress occur respectively.

4.4. Effects of Deformation Amplitude and Frequency

In order to investigate the effects of deformation amplitude and frequency, the mechanical strain, ε, is increased up to 20% while the frequency, f, remains at

0.15 Hz in Case D. On the contrary, the mechanical strain, ε, remains at 10% while the frequency, f, is increased up to 0.30 Hz in Case E. In Case D, the streamlines and velocity vectors are shown in Fig. 24 and the contours of shear stress are shown in Fig. 25 at nine different time points in a deformation cycle. Similarly, in Case E, the streamlines and velocity vectors are shown in Fig. 26 and the contours of shear stress are shown in Fig. 27 at nine different time points in a deformation cycle.

It should be noted that the ranges of velocity in both Fig. 24 and Fig. 26 are the same as those in Fig. 17 and the ranges of shear stress in both Fig. 25 and Fig. 27 are the same as those in Fig. 18 in order to make it easy to observe the differences between Cases C, D and E.

It is revealed that when the mechanical strain and frequency increase, the flow velocity and shear stress also increase during both expansion and contraction. This is because both mechanical strain and frequency appear as parts of the coefficient in Eq. (11). Additionally, it can be noticed that the stagnation points in both Cases D and E are closer to the inlet, as can be seen at time points b – d in Fig. 24 and Fig. 26 respectively, compared to Case C.
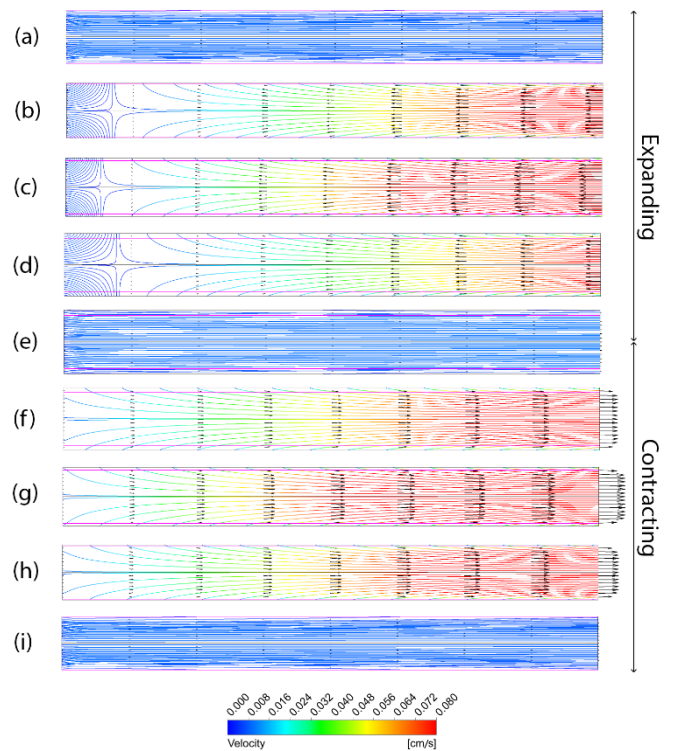
Fig. 24 Streamlines (colorized) and velocity vectors (black) at the top surface in Case D at nine different time points (a – i) during a deformation cycle.
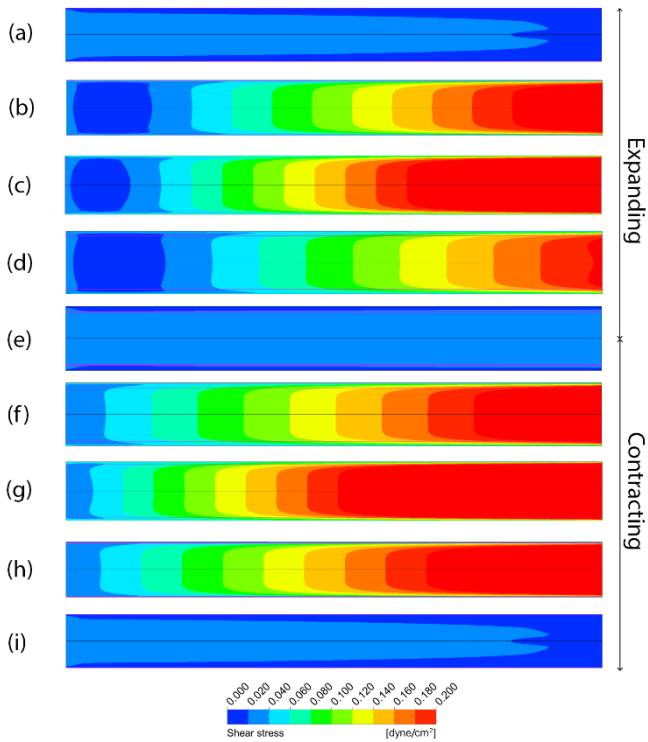
Fig. 25 Contours of shear stress at the bottom surface in Case D at nine different time points (a – i) during a deformation cycle.
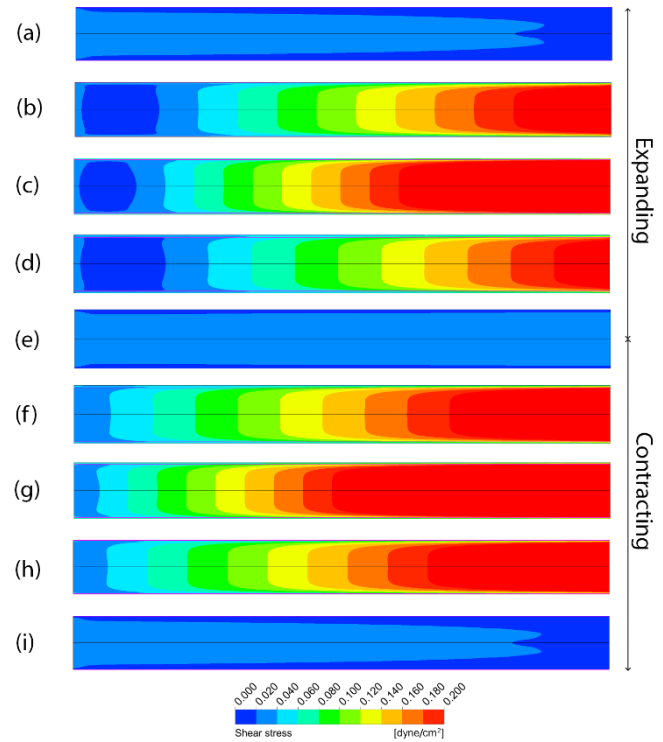
Fig. 27 Contours of shear stress at the bottom surface in Case E at nine different time points (a – i) during a deformation cycle.

In order to further investigate the effect of deformation amplitude and frequency, the shear stress along the AE, BB′, CC′ and DD′ lines in Cases D and E are plotted together with those in Case C as shown in Fig. 28 – Fig. 31 respectively. However, only five time points (a, c, e, g and i) are considered to distinguish the difference between the cases.
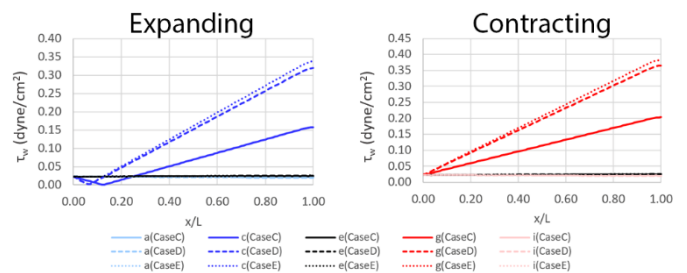
Fig. 28. Plots of shear stress in Case C (solid lines), Case D (dashed lines) and Case E (dotted lines) along the AE line at five different time points (a, c, e, g and i) during a deformation cycle.

Fig. 26 Streamlines (colorized) and velocity vectors (black) at the top surface in Case E at nine different time points (a – i) during a deformation cycle.
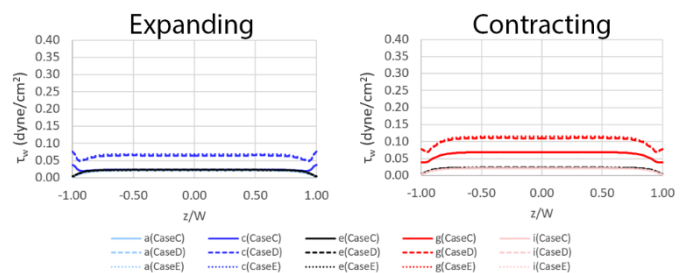
Fig. 29. Plots of shear stress in Case C (solid lines), Case D (dashed lines) and Case E (dotted lines) along the BB′ line at five different time points (a, c, e, g and i) during a deformation cycle.
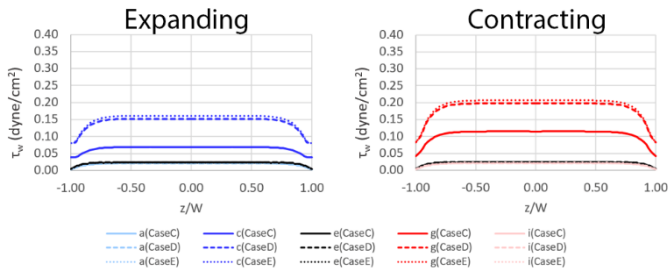
Fig. 30. Plots of shear stress in Case C (solid lines), Case D (dashed lines) and Case E (dotted lines) along the CC′ line at five different time points (a, c, e, g and i) during a deformation cycle.
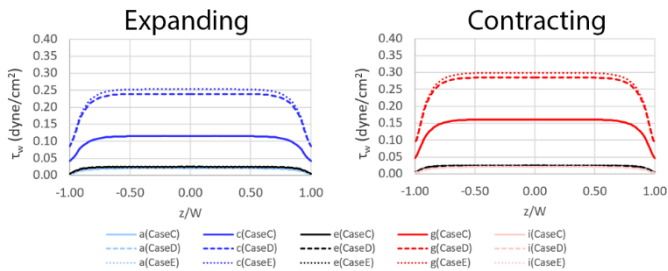
Fig. 31. Plots of shear stress in Case C (solid lines), Case D (dashed lines) and Case E (dotted lines) along the DD′ line at five different time points (a, c, e, g and i) during a deformation cycle.

By comparing the shear stress profiles between Cases C, D and E, the results show that when the sidewalls are at the original position (time points a and i) and at the maximum deformation (time point e), the shear stress profiles are identical in all three cases. However, during the expansion (time point c) and contraction (time point g), even though the shear stress profiles are very similar, the magnitude in Case E is slightly greater than that of Case D, while both Cases D and E gain much greater magnitudes compared to Case C.

To quantify these differences, the area-weighted average shear stresses at the bottom surface, $\overline{\tau_w}$, in Cases C, D and E are plotted together on the primary axis (left axis) and the ratios of $\overline{\tau_w}$ between Cases D and C as well as Cases E and C are plotted on the secondary axis (right axis) as shown in Fig. 32. It is revealed that although the mechanical strain of Case D is twice greater than that of Case C and the frequency of Case E is twice greater than that of Case C throughout a deformation cycle, the ratios of $\overline{\tau_w}$ are not always equal to two. The ratios mostly range between 2.0 and 2.5 during the expansion, while they are mostly between 1.5 and 2.0 during the contraction. The time-averaged shear stresses at the bottom surface during a deformation cycle, $\overline{\overline{\tau_w}}$, in Cases D and E are 0.1071 dyne/cm² and 0.1118 dyne/cm², which are approximately 1.84 times and 1.91 times greater than that of Case C respectively. It should be noted that Fig. 32 is plotted versus a percentage of deformation cycle. However, when the frequency is doubled in Case E, not only the shear stress is increased,

the deformation happens twice as fast compared to Cases C and D as shown in Fig. 33.
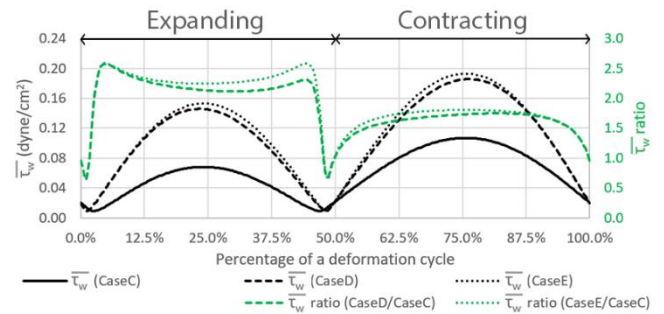
Fig. 32 Plots of area-weighted average shear stress at the bottom surface in Case C (solid lines), Case D (dashed lines) and Case E (dotted lines) with their corresponding ratios during a deformation cycle.
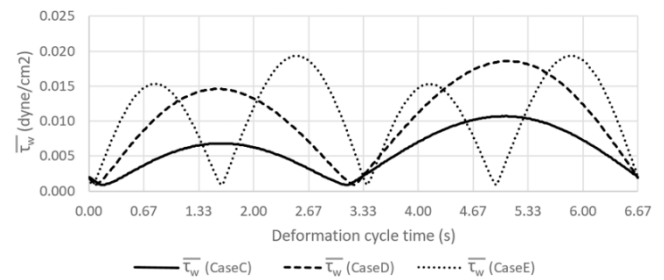
Fig. 33 Plots of area-weighted average shear stress at the bottom surface in Case C (solid lines), Case D (dashed lines) and Case E (dotted lines) on the true time scale.

By breaking the simulation into five separate cases, the shear stress behaviors due to the effects of fluid flow and deforming surfaces are clearly distinguishable. In Case A, where only the main flow is present, it is revealed that the shear stress distributes evenly across the membrane surface on the bottom. From the simulation, the area-weighted average shear stress, $\overline{\tau_w}$, in this case is equal to 0.0210 dyne/cm² which is in good agreement with the shear stress reported earlier by Kim et. al (2012) at 0.02 dyne/cm² [5]. In Case B, where the main flow is absent and the cyclic deformation of the microchannel generated by transversely moving sidewalls is present which induces the secondary flow, the shear stress is low in the middle region and linearly increases toward both ends of the device during both expansion and contraction. In this case, the time-averaged shear stress during a deformation cycle, $\overline{\overline{\tau_w}}$, is equal to 0.0282 dyne/cm². It should be noted that the shear stress due to the cyclic deformation alone is even greater than that due to the main flow, even though the size of microchannel and deformation amplitude are relatively small. In Case C, where both main flow and cyclic deformation are present, the CFD simulation result reveals that the shear stress is greater than 0.02 dyne/cm² most of the time. During the expansion, the shear stress only drops below 0.02 dyne/cm² for a short time after the sidewalls start to expand and before the sidewalls reach the maximum deformation. The time-averaged shear stress during a deformation cycle, $\overline{\overline{\tau_w}}$, is equal to 0.0589 dyne/cm²

which is approximately three times greater than the average shear stress due to the fluid flow alone in case of the stationary microchannel. Furthermore, in Case D where its mechanical strain is twice larger than that of Case C, the simulation reveals that the time-averaged shear stress during a deformation cycle is approximately 1.84 times larger. Finally, in Case E where its frequency is twice larger than that of Case C, the result shows that the behavior occurs twice as fast and the time-averaged shear stress during a deformation cycle is approximately 1.91 times larger.

Additionally, according to the behavior of the shear stress in Cases C, D and E, which varies linearly along the flow path. It is speculated that it is possible to utilize the device that has the streamline-shape microchannel to generate the similar flow pattern and shear stress behaviors by controlling the flow rate within the device such that the shear stress profile is time-dependent. Such device was proposed in 1993 [41] and was used recently to investigate the characteristic of Caco-2 cells as a function of shear stress [32], [42], although there is only one compartment in the device used in these studies and the peristalsis motion is absent.

Finally, in order to estimate the cell shear stress, τ_c, an approximation that treats the cell as a bulge-body [43] is sometimes applied by researchers; however, only the wall shear stress, τ_w, is discussed in this study.

5. Conclusion

This study clearly reveals the behaviors of flow and shear stress in the gut-on-a-chip device subjected to the cyclic deformation of the microchannel in the transverse direction to the main flow. The CFD simulation shows that even though the microchannel length does not appear in the shear stress formula (Eq. (4)), the shear stress actually varies linearly along the microchannel length when the flow is disturbed by the deformation of the membrane and the moving sidewalls. The average shear stress in the present gut-on-a-chip device subjected to the cyclic deformation is approximately three times greater than that of the stationary microchannel. Further investigation also reveals that, by increasing the mechanical strain twice, the average shear stress is increased by the factor of 1.84. Additionally, by doubling the deformation frequency, the average shear stress is increased by the factor of 1.91 and the overall phenomenon happens twice during the same amount of time. The highly dynamic range of shear stress experienced by the Caco-2 cells in the present gut-on-a-chip device could be one of the key mechanisms that accelerates cell differentiation and enriches their characteristic and thus making the dynamic gut-on-a-chip model superior to the traditional static cell culture model.

References

[1] E. W. Esch, A. Bahinski, and D. Huh, "Organs-on-chips at the frontiers of drug discovery," *Nat Rev Drug Discov*, vol. 14, no. 4, pp. 248–260, 2015.

[2] D. Huh, G. A. Hamilton, and D. E. Ingber, "From 3D cell culture to organs-on-chips," *Trends Cell Biol*, vol. 21, no. 12, pp. 745–754, Dec. 2011.

[3] S. N. Bhatia and D. E. Ingber, "Microfluidic organs-on-chips," *Nat Biotechnol*, vol. 32, no. 8, pp. 760–772, 2014.

[4] D. Huh et al., "A human disease model of drug toxicity-induced pulmonary edema in a lung-on-a-chip microdevice," *Sci Transl Med*, vol. 4, no. 159, Nov. 2012.

[5] H. J. Kim, D. Huh, G. Hamilton, and D. E. Ingber, "Human gut-on-a-chip inhabited by microbial flora that experiences intestinal peristalsis-like motions and flow," *Lab Chip*, vol. 12, no. 12, pp. 2165–2174, 2012.

[6] N. S. Bhise et al., "A liver-on-a-chip platform with bioprinted hepatic spheroids," *Biofabrication*, vol. 8, no. 1, Jan. 2016.

[7] K. J. Jang et al., "Human kidney proximal tubule-on-a-chip for drug transport and nephrotoxicity assessment," *Integrative Biology (United Kingdom)*, vol. 5, no. 9, pp. 1119–1129, Sep. 2013.

[8] M. B. Esch, H. Ueno, D. R. Applegate, and M. L. Shuler, "Modular, pumpless body-on-a-chip platform for the co-culture of GI tract epithelium and 3D primary liver tissue," *Lab Chip*, vol. 16, no. 14, pp. 2719–2729, 2016.

[9] J. A. Brown et al., "Recreating blood-brain barrier physiology and structure on chip: A novel neurovascular microfluidic bioreactor," *Biomicrofluidics*, vol. 9, no. 5, Sep. 2015.

[10] I. Maschmeyer et al., "A four-organ-chip for interconnected long-term co-culture of human intestine, liver, skin and kidney equivalents," *Lab Chip*, vol. 15, no. 12, pp. 2688–2699, Jun. 2015.

[11] C. Tian, S. Zheng, X. Liu, and K. Kamei, "Tumor-on-a-chip model for advancement of anti-cancer nano drug delivery system," *J Nanobiotechnology*, vol. 20, no. 1, p. 338, Dec. 2022.

[12] N. Manafi *et al.*, "Organoids and organ chips in ophthalmology," *Ocular Surface*, vol. 19, pp. 1–15, Jan. 2021.

[13] A. Varone *et al.*, "A novel organ-chip system emulates three-dimensional architecture of the human epithelia and the mechanical forces acting on it," *Biomaterials*, vol. 275, Aug. 2021

[14] Y. Baert *et al.*, "A multi-organ-chip co-culture of liver and testis equivalents: A first step toward a systemic male reprotoxicity model," *Human Reproduction*, vol. 35, no. 5, pp. 1029–1044, May 2020.

[15] A. P. Ramme *et al.*, "Autologous induced pluripotent stem cell-derived four-organ-chip," *Future Sci OA*, vol. 5, no. 8, 2019.

[16] R. E. Young and D. D. Huh, "Organ-on-a-chip technology for the study of the female reproductive system," *Advanced Drug Delivery Reviews*, vol. 173, pp. 461–478, Jun. 2021.

[17] A. Bein *et al.*, "Microfluidic organ-on-a-chip models of human intestine," *Cell Mol Gastroenterol Hepatol*, vol. 5, no. 4, pp. 659–668, 2018.

[18] W. Shin, C. D. Hinojosa, D. E. Ingber, and H. J. Kim, "Human intestinal morphogenesis controlled by transepithelial morphogen gradient and flow-dependent physical cues in a microengineered gut-on-a-chip," *iScience*, vol. 15, pp. 391–406, 2019.

[19] M. Kasendra *et al.*, "Development of a primary human small intestine-on-a-Chip using biopsy-derived organoids," *Sci Rep*, vol. 8, no. 1, pp. 1–14, 2018.

[20] T. Murakami, "Absorption sites of orally administered drugs in the small intestine," *Expert Opin Drug Discov*, vol. 12, no. 12, pp. 1219–1232, Dec. 2017.

[21] B. Homayun, X. Lin, and H. J. Choi, "Challenges and recent progress in oral drug delivery systems for biopharmaceuticals," *Pharmaceutics*, vol. 11, no. 3, Mar. 2019.

[22] H. J. Kim and D. E. Ingber, "Gut-on-a-Chip microenvironment induces human intestinal cells to undergo villus differentiation," *Integrative Biology*, vol. 5, no. 9, pp. 1130–1140, Sep. 2013.

[23] S. W. Kim *et al.*, "Shear stress induces noncanonical autophagy in intestinal epithelial monolayers," *Mol Biol Cell*, vol. 28, no. 22, pp. 3043–3056, 2017.

[24] W. Shin and H. J. Kim, "Intestinal barrier dysfunction orchestrates the onset of inflammatory host-microbiome cross-talk in a human gut inflammation-on-a-chip," *Proc Natl Acad Sci USA*, vol. 115, no. 45, pp. E10539–E10547, Nov. 2018.

[25] H. Y. Tan, S. Trier, U. L. Rahbek, M. Dufva, J. P. Kutter, and T. L. Andresen, "A multi-chamber microfluidic intestinal barrier model using Caco-2 cells for drug transport studies," *PLoS One*, vol. 13, no. 5, pp. 1–23, 2018.

[26] C. A. M. Fois, A. Schindeler, P. Valtchev, and F. Dehghani, "Dynamic flow and shear stress as key parameters for intestinal cells morphology and polarization in an organ-on-a-chip model," *Biomed Microdevices*, vol. 23, no. 4, Dec. 2021.

[27] W. Shin and H. J. Kim, "3D in vitro morphogenesis of human intestinal epithelium in a gut-on-a-chip or a hybrid chip with a cell culture insert," *Nat Protoc*, vol. 17, no. 3, pp. 910–939, Mar. 2022.

[28] D. Huh, B. D. Matthews, A. Mammoto, M. Montoya-Zavala, H. Y. Hsin, and D. E. Ingber, "Reconstituting organ-level lung functions on a chip," *Science (1979)*, vol. 328, no. 5986, pp. 1662–1668, 2010.

[29] Y. A. Çengel and J. M. Cimbala, *Fluid Mechanics: Fundamentals and Applications*, 1st ed. McGraw-Hill, 2004.

[30] B. R. Munson, D. F. Young, T. H. Okiishi, and W. W. Huebsch, *Fundamentals of Fluid Mechanics*, 6th ed. Wiley, 2009.

[31] M. H. Chaudhry, *Applied Hydraulic Transients*, 3rd ed. Springer New York, 2014.

[32] L. C. Delon *et al.*, "A systematic investigation of the effect of the fluid shear stress on Caco-2 cells towards the optimization of epithelial organ-on-chip models," *Biomaterials*, vol. 225, Dec. 2019.

[33] X. Zhang, P. Jones, and S. J. Haswell, "Attachment and detachment of living cells on modified microchannel surfaces in a microfluidic-based lab-on-a-chip system," *Chemical Engineering Journal*, vol. 135, no. SUPPL. 1, Jan. 2008.

[34] J. Y. Park *et al.*, "Single cell trapping in larger microwells capable of supporting cell spreading and proliferation," *Microfluid Nanofluidics*, vol. 8, no. 2, pp. 263–268, Feb. 2010.

[35] A. Siddique, T. Meckel, R. W. Stark, and S. Narayan, "Improved cell adhesion under shear stress in PDMS microfluidic devices," *Colloids Surf B Biointerfaces*, vol. 150, pp. 456–464, Feb. 2017.

[36] S. V. Patankar, *Numerical Heat Transfer and Fluid Flow*, 1st ed. McGraw-Hill, 1980.

[37] ANSYS Inc., *ANSYS Fluent Theory Guide*, Release 2019 R3. 2019.

[38] P. Borwornpiyawat *et al.*, "Effects of porous size and membrane pattern on shear stress characteristic in gut-on-a-chip with peristalsis motion," *Micromachines*, vol. 14, no. 1, p. 22, 2023.

[39] K. Kulthong *et al.*, "Microfluidic chip for culturing intestinal epithelial cell layers: Characterization and comparison of drug transport between dynamic and static models," *Toxicology in Vitro*, vol. 65, pp. 104815, Feb. 2020.

[40] R. Courant, K. Friedrichs, and H. Lewy, "On the partial difference equations of mathematical physics," *IBM J Res Dev*, vol. 11, no. 2, pp. 215–234, Mar. 1967.

[41] S. Usami, H. H. Chen, Y. Zhao, S. Chien, and R. Skalak, "Design and construction of a linear shear stress flow chamber," *Ann Biomed Eng*, vol. 21, no. 1, pp. 77–83, 1993.

[42] L. C. Delon, Z. Guo, M. N. Kashani, C.-T. Yang, C. Prestidge, and B. Thierry, "Hele Shaw microfluidic device: A new tool for systematic investigation into the effect of the fluid shear stress for organs-on-chips," *MethodsX*, vol. 7, 2020.

[43] D. P. Gaver and S. M. Kute, "A theoretical model study of the influence of fluid stresses on a cell adhering to a microchannel wall," *Biophys J*, vol. 75, no. 2, pp. 721–733, 1998.

———————— • ————————

Pannasit Borwornpiyawat received B.Eng. degree in mechanical engineering from Kasetsart University, Thailand in 2014 and received M.Eng. degree in mechanical and automotive engineering from King Mongkut's University of Technology North Bangkok, Thailand in 2016. During his Master degree, he also worked as a research assistance and developed a computational fluid dynamics (CFD) solver for Thailand National Metal and Materials Technology Center (MTEC), National Science and Technology Development Agency (NSTDA). Since 2017, he has been a Ph.D. candidate in Mechanical Engineering Simulation and Design (MESD) group at The Sirindhorn International Thai-German Graduate School of Technology (TGGS), King Mongkut's University of Technology North Bangkok (KMUTNB), Thailand. During his doctoral study, he receives the Thailand Graduate Institute of Science and Technology (TGIST) scholarship from NSTDA and he is also a teaching assistance in C/C++ programming and CFD classes. His research interests are numerical methods, CFD, microfluidics and organ-on-a-chip applications.

Ekachai Juntasaro received B.Eng. degree in mechanical engineering from King Mongkut's Institute of Technology Ladkrabang (KMITL), Thailand, in 1989, and pursued both M.Sc. and Ph.D. degrees in mechanical engineering at Imperial College London, U.K., in 1992 and 1997 respectively with the Royal Thai Government Scholarship. In 1997, he started working as Lecturer at School of Mechanical Engineering, Institute of Engineering, Suranaree University of Technology (SUT), Nakhon Ratchasima, Thailand, where he became Assistant Professor and Associate Professor in 2001 and 2006 respectively. Since 2008, he has worked as Associate Professor in Mechanical Engineering Simulation and Design (MESD) Group at The Sirindhorn International Thai-German Graduate School of Engineering (TGGS), King Mongkut's University of Technology North Bangkok (KMUTNB), Thailand. His research interests are transition and turbulence modelling with/without analytical wall function (AWF), unstructured finite volume method for computational fluid dynamics (CFD), microfluidics, and turbomachinery flow in power plants.

Sasitorn Aueviriyavit received B.Sc. degree in Pharmaceutical Sciences (First class honours) from Chulalongkorn University, Thailand, in 2002, and received M.Sc. and Ph.D. degrees in Pharmaceutical Sciences from Graduate School of Medical and Pharmaceutical Sciences, Chiba University, Japan in 2007 and 2010, respectively with the Japanese government scholarship. In 2010, she became the researcher at Nano Safety and Risk Assessment Laboratory at National Nanotechnology Center (NANOTEC), National Science and Technology Development Agency (NSTDA), Thailand. Currently, she is the team leader of Nano Safety and Bioactivity Research Team (NSB), NANOTEC. Her research interests are the development of an advanced predictive model that plays an important role to bridge the gap in the state-of the-art technologies in toxicity and efficacy prediction and molecular/mechanism studies of nanomaterials and bioactive compounds.

Varangrat Juntasaro received B.Eng. and Ph.D. degrees in mechanical engineering from Imperial College London, U.K., in 1995 and 1999 respectively with the Royal Thai Government Scholarship. In 1999, she started working as Lecturer at Department of Mechanical Engineering, Faculty of Engineering, Kasetsart University, Bangkok, Thailand, where she became Assistant Professor and Associate Professor in 2001 and 2006 respectively. Her research interests are computational fluid dynamics (CFD), turbulence modelling, and turbomachinery flow in power plants.

Witsaroot Sripumkhai received M.S. degree in science and nanotechnology from College of Nanotechnology, KMITL, Thailand. He is currently a Senior Assistant Researcher in Surface and Microfluidic Device Innovation Research Team at Thai Microelectronics Center (TMEC), NECTEC, NSTDA. His research interests are microfabrication process for microfluidic applications and superhydrophobic surface for antifouling application.

Pattaraluck Pattamang received M.S. degree in science and nanotechnology from College of Nanotechnology, KMITL, Thailand. She is currently an Assistant Researcher in Surface and Microfluidic Device Innovation Research Team at Thai Microelectronics Center (TMEC), NECTEC, NSTDA. Her research interests are microfluidic device and lab on a disk.

Rattanawan Meananeatra received her Bachelor's degree in Electrical Engineering from King Mongkut's Institute of Technology North Bangkok, Thailand in 2004 and Master's degree in Microelectronics Engineering from King Mongkut's Institute of Technology Ladkrabang, Thailand in 2010. Her research focuses on Si-based semiconductor process technology, micro/nano patterning, microfluidic devices, and superamphiphobic and anti-fouling surface by surface texturing and modification for various applications.

Kornphimol Kulthong received her B.Sc. degree in Chemistry from Srinakharinwirot University in 2000. Afterwards, she worked as R&D for 5 years in the cosmetic industry and decided to pursue M.Sc. degree in Pharmacology at Chulalongkorn University with the thesis related to drug metabolism enzymes (2005-2008). She has been working for National Nanotechnology Centre in Thailand (Ministry of Higher Education, Science, Research, and Innovation) since 2008 and got a scholarship from the Royal Thai Government in 2015 to be a Ph.D. candidate at the division of Toxicology of Wageningen University & Research. She received her Ph.D. degree in 2020 and returned to Thailand to continue her job at National Nanotechnology Centre with the aim of implementing an in vitro model for toxicity testing.

Ratjika Wongwanakul received her Bachelor's degree in Pharmacy from the Faculty of Pharmacy, Srinakharinwirot University, Bangkok, Thailand in 2008 and Master's degree in Pharmacology from the Faculty of Pharmaceutical Science at Chulalongkorn University in 2012. Then, she got the educational grant supporting of Ph.D. study by Thailand Graduate Institute of Science and Technology (TGIST) and graduated from the Faculty of Pharmaceutical Science at Chulalongkorn University with a degree in the Doctor of Philosophy in Biopharmaceutical Sciences in 2016. After that, she was a Postdoctoral Fellow for 8 months at Chulalongkorn University Drug & Health Products Innovation Promotion Center, Thailand and further worked as a NSTDA co-researcher, Safety and Risk Assessment Laboratory, National Nanotechnology Center (NANOTEC), National Science and Technology Development Agency (NSTDA), Thailand until March 2019. Since April 2019, she has been worked as a researcher at Nano Safety and Bioactivity Research Team, NANOTEC, NSTDA, Thailand. Her research interest includes development of 3D-tissue model using organoid culture generated from adult stem cells and its applications, focusing on 3D-intestinal model.

Numfon Khemthongcharoen received her Bachelor's and Master's degrees in medical technology, Mahidol University. In 2015, she won the Royal Golden Jubilee Ph.D. Program scholarship granted by the Thailand Research Fund. She received her Ph.D. in Biomedical Engineering from Faculty of Engineering, Mahidol University in 2021. She has worked at National Electronics and Computer Technology Center (NECTEC), Thailand since 2010. Her research interests are biosensors, Bio-Optics, microfluidic system, and optical devices for medical diagnosis.

Panut Bumphenkiattikul received his Bachelor's degree and Master's degree in Chemical Engineering from Kasetsart University in Bangkok, Thailand, and has conducted research on topics such as polypropylene in fluidized bed reactors and hydrodynamic in trickle bed reactors. During his time studying for his Master's degree, he was also part of a chemicals reaction and flow phenomena consulting team for petrochemical industrial research projects. From 2015 to 2016, he served as a visiting researcher at the Department of Energy, Environmental & Chemical Engineering at Washington University in St. Louis, MO, USA. Since October 2018, he has been working as a CAE and CFD Simulation Engineer at SCGC, where he develops CFD models for plant equipment design optimization and analyzes fluid flow phenomena for process modification.

Arthit Vongachariya received B.S. and M.S. degree in chemistry of science from Chulalongkorn University, Bangkok, Thailand in 2008 and 2010 respectively. From 2010 to 2016, he was as researcher with Ube Technical Center (Asia) Limited. From 2016 to 2020, he has been lead engineer with process technology center department, SCG Chemicals, Thailand. Since 2020, he has been promoted as CAE and CFD team leader with digital manufacturing department, SCG Chemicals that technical support process and product development in petrochemical business. He also in charged of HPC implementation in SCG Chemicals along the process from starting to end user application. He worked closely on various simulation techniques which running on HPC along his career.

Nithi Atthi received his Bachelor's degree in Materials Engineering and Master's degree in Engineering Management from Kasetsart University (KU) in 2004 and 2008. In 2013, he won the MEXT Monbukagakusho scholarship granted by the Japanese Government to pursue his graduate study at the Tokyo Institute of Technology and received his master's degree and Ph.D. in Electronics and Applied Physics. He was awarded as the Green Talent Fellow (Germany) in 2018, the 10th HOPE Meeting Fellow (Japan) in 2018, the Young Leaders of the 16th STS forum (Japan) in 2019, and the Leaders in Innovation Fellowships (LIF Programme, United Kingdom) in 2022. He has authored and co-authored more than 44 technical journal publications, given a talk on his research at more than 122 academic conferences, and filed 27 domestic and international patents. In 2018, he was appointed as a Research Team Leader of the Surface and Microfluidic Device Innovation Research Team at the Thai Microelectronics Center (TMEC), Thailand. His research focuses on Si-based semiconductor process technology, micro/nano-patterning, high-k/metal gate stacks, microfluidic devices, and superamphiphobic and anti-fouling surfaces by surface texturing and modification for various applications.

Wutthinan Jeamsaksiri received Master's degree and Ph.D. in Electrical and Electronic Engineering from Imperial College, London. He is now holding a position as a director of Thai Microelectronics Center (TMEC) overseeing collaborative R&D activities as well as commercialization of technology platforms from all research teams; The platforms include industrial Si MEMS, ISFET for plant factory and medical applications, microfluidic devices for high throughput low cost medical applications, super clean surface by means of superamphiphobic technology.